Impact Energy Measurement in Time-of-Flight Mass Spectrometry with Cryogenic Microcalorimeters *

G. C. Hilton[†], John M. Martinis[†], D. A. Wollman[†], K. D. Irwin[†], L. L. Dulcie[†], Daniel Gerber[‡], Patrick M. Gillevet[§], & Damian Twerenbold[‡]

[†]National Institute of Standards and Technology, Boulder CO, 80303
[‡]Institut de Physique de l'Université Rue A.-L. Breguet 1, CH-2000 Neuchâtel, Switzerland and GenSpec SA, case postale 120, CH-2017 Boudry, Switzerland
[§]Institute of Bioscience, Bioinformatics, and Biotechnology, George Mason University, Manassas, VA 22210

Time-of-flight mass spectrometry, most notably matrix-assisted laser-desorption-ionization time-of-flight (MALDI-TOF) spectrometry,[1] are important techniques in the study of proteins and other biomolecules.[2] While these techniques provide excellent performance for masses up to about 20 kDa, there has been limited success in achieving good mass resolution at higher masses. The sensitivity of conventionally used microchannel plate (MCP) detectors decreases rapidly with increasing particle mass, limiting the utility of MCP detectors for very large masses. It has been proposed that cryogenic particle detectors may provide a solution to these difficulties.[3] Unlike MCP detectors, which measure the multiplied ion current initiated by a secondary electron or ion, cryogenic detectors measure the thermal energy deposited by the particle impact, and thus have a sensitivity that is largely independent of particle mass. Recent experiments[4–6] have demonstrated the sensitivity of cryogenic particle detectors to single biomolecules, a quantum efficiency several orders of magnitude larger than the MCP detectors, and sensitivity to masses as large as 750 kDa. In this paper we present results demonstrating an order of magnitude better energy resolution than previous measurements, allowing direct determination of particle charge state during acceleration.[7] We also present calibrated measurements of ion impact energy and measurements demonstrating particle energy loss due to gas-phase collisions in the spectrometer.

In the past several years, significant progress has been made in developing high-performance cryogenic detectors for applications such as infrared bolometry and x-ray, visible, and ultraviolet spec-

*Contribution of the U.S. Government, not subject to copyright.

troscopy. These detectors fall into two classes: non-equilibrium devices such as superconducting tunnel junctions (STJs),[8,9] and equilibrium devices such as microcalorimeters.[10–13] The previous experiments with cryogenic particle detectors for mass spectrometry used STJs,[4,5] which fail to record the total impact energy because they are insensitive to the fraction of impact energy deposited as phonons with energy less than the superconducting gap. In this experiment we used a normal-insulator-superconductor (NIS) microcalorimeter fabricated on a thin Si_3N_4 membrane which detects all of the thermal energy deposited by a particle impact. Although the speed and energy resolution performance of our detector is sufficient for this preliminary experiment, experience with other applications indicate that significantly better performance is possible in the future. It is important to note that the collection area of the cryogenic detectors studied is more than 10^4 times smaller that typical MCP detectors. While this size can be improved in the future, the overall sensitivity (the product of quantum efficiency and collection area) of this detector is significantly less than MCP detectors except at extremely large masses.[6]

Our detector, similar to that described elsewhere,[12] is shown in cross section in figure 1a, along with the external circuit used to bias and read out the detector. The detector current is measured using a high-speed low-noise series-array superconducting quantum interference device (SQUID) amplifier.[14] The detector is cooled to its operating temperature of 100 mK using a liquid helium cryostat with an adiabatic demagnetization refrigerator. The cryostat is coupled to a MALDI-TOF spectrometer as shown in figure 1b.

The detector energy scale was calibrated using x-rays from a ^{55}Fe radioactive source mounted in the detector line of sight. The energy resolution of detector was measured for x-rays using several thousand digitized waveforms. The energy of each event was determined using Weiner optimal filtering, and the resolution was determined by fitting the resulting energy histogram to a normal distribution. For x-rays we obtained an energy resolution of 92 eV full width at half maximum (FWHM). In figure 2a we show a digitized detector waveform obtained from one laser strike on a protein target of bovine serum albumin (BSA, mass = 66430 Da).

In figure 2b we show a scatter plot of impact energies *vs.* arrival times for a sample of BSA in a sinapinic acid matrix (mass = 224 Da). The plot demonstrates a clear energy banding, caused by the discrete ionization states of the particles. The utility of impact energy resolution is clearly shown by examining two groupings of points, one at (t_1=146 μs, E_1=10 keV), and the other at (t_2=103 μs, E_2=20 keV). Calculating the mass corresponding to t_1 using $m = (2zUt^2)/l^2$ where l is the length of the flight tube and taking $z = e$, we find that m_1=66.6 kDa. If we similarly calculate the mass corresponding to t_2 with z=2e, we find m_2=66.4 kDa. Thus we associate the first grouping with BSA$^+$ and the second grouping with BSA^{2+}. Additional groupings in figure 2b include sinapinic acid (m=224 Da, t=10 μs) and an unidentified fragment with $m \approx$14 kDa (t=67 μs). There is also a small grouping at the same time-of-flight as the BSA$^+$ group with twice the energy of the BSA$^+$ group. This group is due to either doubly charged BSA dimers or the simultaneous arrival of two singly charged BSA monomers.

A surprising feature of figure 2b is that the thermal energy E_d deposited in the microcalorimeter by a particle impact is roughly half of the particle's kinetic energy zU. This difference implies that a significant fraction of the particle's kinetic energy is not converted to thermal energy in the detector. Thus impact cannot be modeled as a rigid molecule striking and sticking to the detector. Processes that might account for the missing energy include fragmentation of the impacting molecule and ejection of molecular fragments.

To further investigate the dependence of impact energy on molecule type, we show in figure 3 the ratio of deposited to kinetic energy *vs.* kinetic energy for three different molecules. At low kinetic energies, we see indications of an increase in fractional energy deposition, as might be expected since there is less energy available to deform the ion. Presumably E_d/zU approaches 1 at very low kinetic energies. At large kinetic energies, the proteins deposit about half of their kinetic energy in the detector, while the much lighter sinapinic acid deposits nearly three-quarters of its kinetic energy. Because there are many more bonds in the larger molecules, it is not surprising that more of the kinetic energy is lost in impact ejection or fragmentation. While we do not fully understand the origin of the asymptotic

50% impact energy observed at high kinetic energies for lysozyme and BSA, preliminary experiments with immunoglobulin G (IgG, 155 kDa) show that this same asymptotic limit holds for larger masses. Because the total bond energy of sinapic acid is less that the impact energy deficit, we believe that this is evidence that ejection is the dominant energy loss mechanism. In the only previous measurement of fractional energy deposition using STJs,[5] the measured impact energy was roughly 20% of the kinetic energy. The lower value of E_d/zU obtained with the STJ detectors is not surprising, given the phonon loss mechanisms previously discussed.

Histograms of arrival times for BSA are plotted in figure 4a using all particle impacts, and in figure 4b using only those events with impact energies between 5 and 15 keV. In the selective plot of 4b, both the background and the BSA^{2+} peak have been greatly reduced. Similar histograms were used to determine the mass and energy resolution of the mass spectrometer. For the BSA monomer peak, we obtain a timing resolution of 1.3 μs (FWHM), implying a mass resolution $M/\Delta M$ of 56, similar to results obtained elsewhere.[15] An energy resolution of 1.7 keV (FWHM) was obtained, which is significantly worse than both the 92 eV (FWHM) resolution obtained with x-rays and the kinetic energy uncertainty implied by the time-of-flight uncertainty, inferring that the energy lost to ejection and fragmentation during impact must be variable.

Measurement of impact energy with the microcalorimeter allows us to explore of the effect of background gas pressure in the spectrometer. As background pressure increases, gas-phase collisions in both the acceleration and free-flight regions increase, decreasing the quality of the spectra. The effect of pressure is clearly demonstrated in figure 5a, which shows scatter-plot spectra for lysozyme (mass = 14300 Da) taken at 4×10^{-5} Pa (3×10^{-7} Torr) and 8×10^{-4} Pa (6×10^{-6} Torr). At high pressure, we observe a significant increase in the number of low energy (less than 5 keV) particles arriving at the predicted time-of-flight for lysozyme. We attribute this effect to fragmentation of the lysozyme ions due to collisions with background gas in the free-flight region of the spectrometer. Fragments produced during free flight carry less kinetic energy, but travel at velocities nearly equal to that of the original molecule and

arrive at the expected time for lysozyme. On the other hand, fragmentation during acceleration would affect the velocity and cannot explain these events. In figure 5b we show the effect on this fragmentation on impact energy. Here we plot a histogram of impact energies for those particle arriving with near the predicted time-of-flight for lysozyme. The histograms show that at low pressure there are many more low energy events which are caused by small fragments, and a broadening of the primary 11 keV peak by a low energy tail which is caused by larger fragments.

Insight into the effect of gas phase collisions can be gained by estimating the cross sections and mean free paths of the proteins. From x-ray structure data for lysozyme,[16] we estimate the molecular cross section for gas-phase scattering to be 15 nm^2. With this cross section, the mean free path for lysozyme at a nitrogen gas pressure of 4×10^{-5} Pa is roughly 6 m, while at 8×10^{-4} Pa the mean free path is 0.3 m. Thus at the higher pressure considered in figure 5 lysozyme will typically undergo 3-4 collisions in traversing the flight tube. Assuming hard-sphere elastic collisions between a 20 keV lysozyme ion and an ambient-temperature nitrogen molecule, the maximum energy transferred per collision is 160 eV. This energy is more than sufficient to break bonds in lysozyme, supporting our conclusion that fragmentation occurs during flight. These results are similar to those reported elsewhere[17] where fragmentation caused in the free flight region was measured by subsequent deceleration of ions, allowing measurement of the relative concentration of neutral fragments relative to unfragmented ions to yield the fragmentation cross section. For a protein similar to lysozyme (cytochrome *c*) they measure a cross section of 14.1 nm^2 consistent with our results.

A similar calculation of the cross section for BSA shows that gas phase collisions cannot explain the mass resolution obtained with our spectrometer. Using x-ray data[18] we estimate the cross section of BSA to be 30 nm^2, giving a mean free path of 3 meters at the normal operating pressure. Assuming that the maximum energy transferred per gas collision is 80 eV, and that each molecule undergoes on average less than one collision, the worst case estimate for mass resolution $M/\Delta M$ is 250, which is s better than the observed value of 56. In the present experiments, where mass resolution is not limited by

gas collisions or detector response time, we conclude that the greatest contributions to mass uncertainty arise during launch and acceleration.

Correspondence and requests for materials to Gene Hilton at hilton@boulder.nist.gov.

References

[1] Karas, M. and Hillenkamp, F. Laser Desorption Ionization of Proteins and Molecular Masses Exceeding 10000 Daltons. *Anal. Chem.* **188**(60), 2299–2301 (1988).

[2] Siuzdak, G. The emergence of mass spectrometry in biochemical research. *Proc. Natl. Acad. Sci. USA* **91**, 11290–11297 November (1994).

[3] Twerenbold, D. Biopolymer mass spectrometer with cryogenic particle detectors. *Nucl. Instrum. Methods Phys. Research A* **370**, 253–255 (1996). US Patent no. 5,640,010.

[4] Twerenbold, D., Vuilleumier, J.-L., Gerber, D., Tadsen, A., van den Brandt, B., and Gillevet, P. M. Detection of single macromolecules using a cryogenic particle detector coupled to a biopolymer mass spectrometer. *Appl. Phys. Lett.* **68**, 3503–3505 (1996).

[5] Frank, M., Mears, C. A., Labov, S. E., and Benner, W. H. High-efficiency Detection of 66 000 Da Protein Molecules Using a Cryogenic Detector in a Matrix-assisted Laser Desorption/Ionization Time-of-flight Mass Spectrometer. *Rapid Comm. in Mass Spectrometry* **10**, 1946 (1996).

[6] Labov, S. E., Frank, M., Lindeman, M. A., Netel, H., Hiller, L. J., Chow, D., Friedrich, S., Mears, C. A., Caldara, G., and Barfknecht, A. T. Cryogenic detector development at LLNL: ultraviolet, X-ray, gamma-ray and biomolecule spectroscopy. *Proceedings of the Seventh International Workshop on Low Temperature Detectors* , 82–95 (1997).

[7] Benner, W. H., Horn, D. M., Jaklevic, J. M., Frank, M., Mears, C., Labov, S., and Barfnecht, A. T. Simultaneous Measurement of Flight Time and Energy of Large Matrix-Assisted Laser Desorption Ions with a Superconducting Tunnel Junction Detector. *J. Am. Soc. Mass Spectrom.* **8**, 1094–1102 (1997).

[8] Mears, C. A., Labov, S. E., Frank, M., Lindeman, M. A., Hiller, L. J., Netel, H., and Barfknecht, A. T. Analysis of pulse shape from a high resolution superconducting tunnel junction X-ray spectrometer. *Nucl. Instrum. Methods Phys. Research A* **370**, 53–56 (1996).

[9] Peacock, A., Verhoeve, P., Rando, N., van Dordrecht, A., Taylor, B. G., Erd, C., Perryman, M. A. C., Venn, R., Howlett, J., Goldie, D. J., Lumley, J., and Wallis, M. Single optical photon detection with a superconducting tunnel junction. *Nature* **381**, 135–137 May (1996).

[10] McCammon, D., Cui, W., Juda, M., Morgenthaler, J., and Zhang, J. Thermal calorimeters for high resolution X-ray spectroscopy. *Nucl. Instrum. Methods Phys. Research A* **326**, 157–165 (1993).

[11] Irwin, K. D., Hilton, G. C., Wollman, D. A., and Martinis, J. M. X-ray detection using a superconducting transition-edge sensor microcalorimeter with electrothermal feedback. *Appl. Phys. Lett.* **69**(13), 1945–1947 (1996).

[12] Nahum, M. and Martinis, J. M. Hot-electron microcalorimeters as high-resolution x-ray detectors. *Appl. Phys. Lett.* **66**, 3203–3205 (1995).

[13] Martinis, J. M. Hot-electron-microcalorimeters with 0.25 mm^2 area. *Nucl. Instrum. Methods Phys. Research A* **370**, 171–172 (1996).

[14] Welty, R. P. and Martinis, J. M. A series array of DC SQUIDs. *IEEE Trans. Mag.* **27**, 2924–2926 (1991).

[15] Schreiner, M., Strupat, K., Lottspeich, F., and Eckershorn, C. Ultraviolet matrix assisted laser desorption ionization-mass spectrometry of electroblotted proteins. *Electrophoresis.* **17**, 954–961 (1996).

[16] Vaney, M. C., Maignan, S., Ries-Kautt, M., and Ducruix, A. Protein Data Bank file number 1931. Brookhaven National Laboratory Protein Data Bank, (1995).

[17] Spengler, B., Kirsch, D., and Kaufmann, R. Fundamental Aspects of Postsource Decay in Matrix-Assisted Laser Desorption Mass Spectrometry. 1. Residual Gas Effects. *J. Phys. Chem.* **96**(24), 9678–9684 (1992).

[18] He, X. M. and Carter, D. C. Atomic structure and chemistry of human serum albumin. *Nature* **358**(358), 209–215 (1992).

Figure Captions

Figure 1. (a) A cross section of the NIS microcalorimeter. An accelerated molecule flies through a 200 μm diameter 0.1 K aperture and strikes the absorber (a 100 nm thick Ag film measuring 200 μm by 200 μm deposited on a 0.5 μm thick Si_3N_4 membrane), raising the absorber temperature. This temperature rise is detected as a current pulse produced by a voltage biased NIS junction, which consists of a thinly oxidized Al electrode in contact with the absorber. The junction current is measured by a SQUID preamplifier. Contacts to the detector are provided by superconducting Al leads which carry electrical current but do not conduct heat. (b) Schematic view of our MALDI-TOF spectrometer indicating detector placement and infrared shielding. The infrared shielding consists of a 1 mm diameter aperture cooled to 4 K and placed 10 cm away from the detector. Ions are created when laser light pulses (337 nm, 3 ns, maximum power 100 μJ) strike the probe plate. Ions are accelerated by an electric field between the probe plate and the grounded fine-mesh accelerating grid. Vacuum in the spectrometer is provided by a 110 L/s turbomolecular pump, attaining a base pressure in the 100 mm diameter flight tube of 2×10^{-5} Pa (1.5×10^{-7} Torr). Two proteins were studied, lysozyme (mass = 14300 Da) and bovine serum albumin (BSA, mass = 66430 Da). In both cases proteins solutions were prepared by combining 1 mg of protein with 1 mL of a 0.1% trifluoroacetic acid H_2O solution. The matrix solution consisted of 100 mg sinapinic acid (mass = 224 Da) dissolved in 6 ml of ethanol and 4 ml H_2O. Probes were prepared by mixing 40 μL each of the probe and matrix solutions and allowing the mixture to air dry on the probe plate.

Figure 2.(a) An example time trace for one laser event with three detector pulses. The first pulse is due to reflected laser light striking the detector, the remaining pulses are due to ions and are identified as BSA^{2+} and BSA^{+}. (b) A scatter plot of detector energy *vs.* ion time-of-flight for BSA with an acceleration voltage of 20 kV. Clear energy banding is shown for ions of different charge. The ratio of energy deposited in the detector to ion kinetic energy (E_d/zU) is 0.59 for BSA^{+} and 0.74 for singly charged sinapinic acid. This scatter plot was generated by extracting time and energy information from time

traces for several thousand laser events. For each laser pulse we acquired a time trace consisting of 4096 samples of the SQUID preamplifier output at either 50 or 100 ns intervals using a 20 MHz 12-bit analog-to-digital converter. Particle impact times were determined by an edge detection algorithm applied to the time traces and particle impact energies were extracted by comparing the impact waveforms with a calibrated waveform derived from x-ray events. The signal rise time (1.2 μs) allowed us to determine the time of impact within roughly 200 ns. Potential difficulties of pulse pile-up due to the slow detector fall time (17 μs) are mitigated by the detector linearity, the 12 bit digitization, and the small number of particle strikes per launch event.

Figure 3. A plot of the ratio of impact energy to kinetic energy *vs.* kinetic energy for each ion type. The ratio is determined by dividing the centroid of the impact energy distribution for an identified particle grouping by the kinetic energy of that grouping. For the heavier ions (lysozyme, BSA) this fraction approaches 0.54 for large acceleration potentials, while for the lighter ion (sinapinic acid) the asymptote is 0.72.

Figure 4. Time-of-flight spectrum for BSA with an acceleration voltage of 20 kV. The upper plot shows the full histogram with all acquired points. The lower plot contains only those points whose deposited energy is between 5 and 15 kV. The peak due to doubly ionized BSA, as well as much of the background, is removed by this selection.

Figure 5. (a) Scatter plots for lysozyme (mass = 14300 Da) taken at two different pressures. At the higher pressure, many more ions with low impact energy are observed. This effect is due to gas phase scattering and fragmentation in the flight tube. The mean free path for lysozyme collision with ambient gas molecules is 1/3 of the flight tube length in the high pressure case and 6 times the flight tube length in the low pressure case. (b) Histogram of impact energies for the expected arrival time of lysozyme$^+$ (68 μs $<$ t $<$ 70 μs). The data at higher pressure show both a low energy peak and an enhanced low energy tail of the 11 keV peak. These features are due to small and large fragments of the lysozyme

caused by gas-phase fragmentation in the free-flight region.

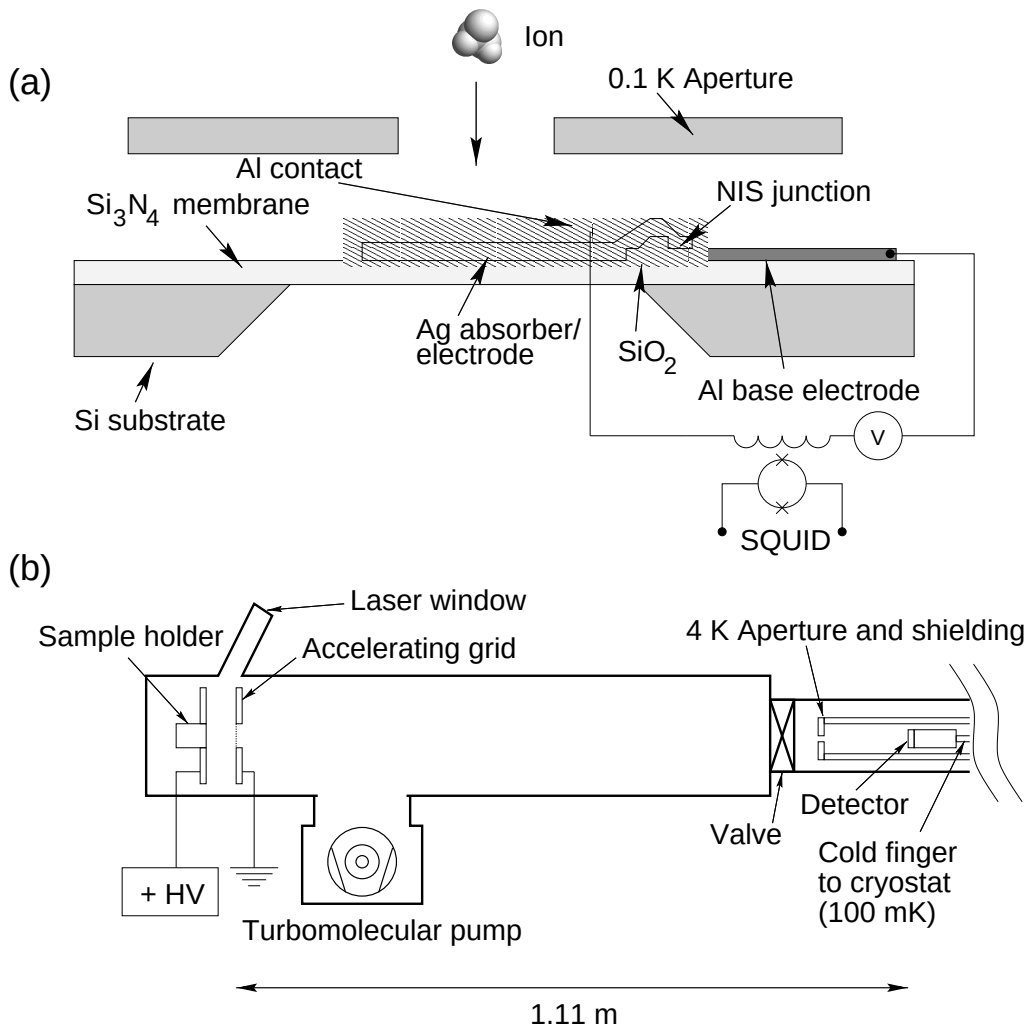
(a)
Ion
0.1 K Aperture
Al contact
Si_3N_4 membrane
NIS junction
Ag absorber/
electrode
SiO_2
Al base electrode
Si substrate
V
SQUID
(b)
Laser window
Sample holder
Accelerating grid
4 K Aperture and shielding
Detector
Valve
Cold finger
to cryostat
(100 mK)
+ HV
Turbomolecular pump
1.11 m

Figure 1.

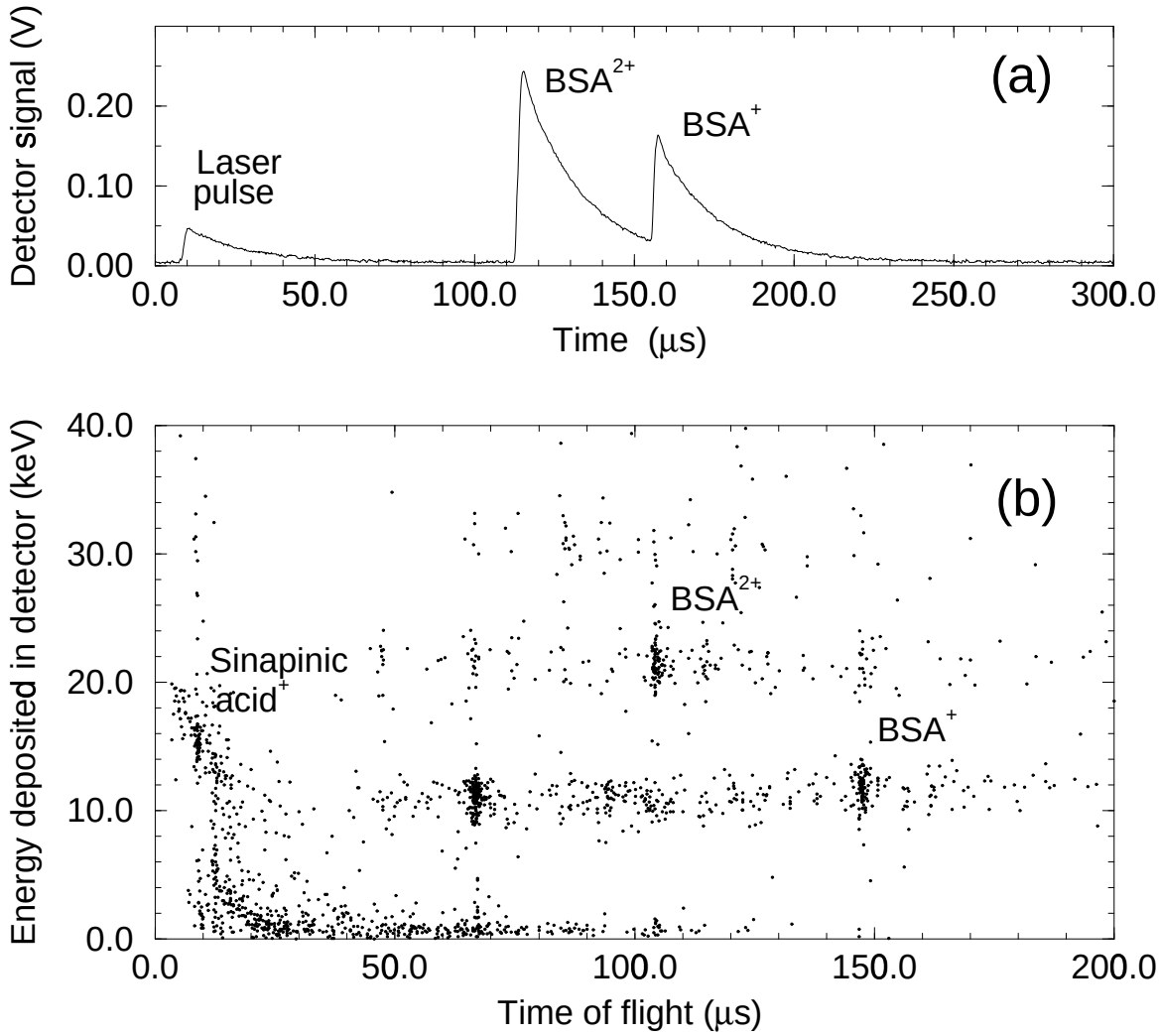
(a)
Detector signal (V)
0.00
0.10
0.20
Laser pulse
BSA2+
BSA+
0.0
50.0
100.0
150.0
200.0
250.0
300.0
Time (μs)
(b)
Energy deposited in detector (keV)
0.0
10.0
20.0
30.0
40.0
Sinapinic acid+
BSA2+
BSA+
0.0
50.0
100.0
150.0
200.0
Time of flight (μs)

Figure 2.

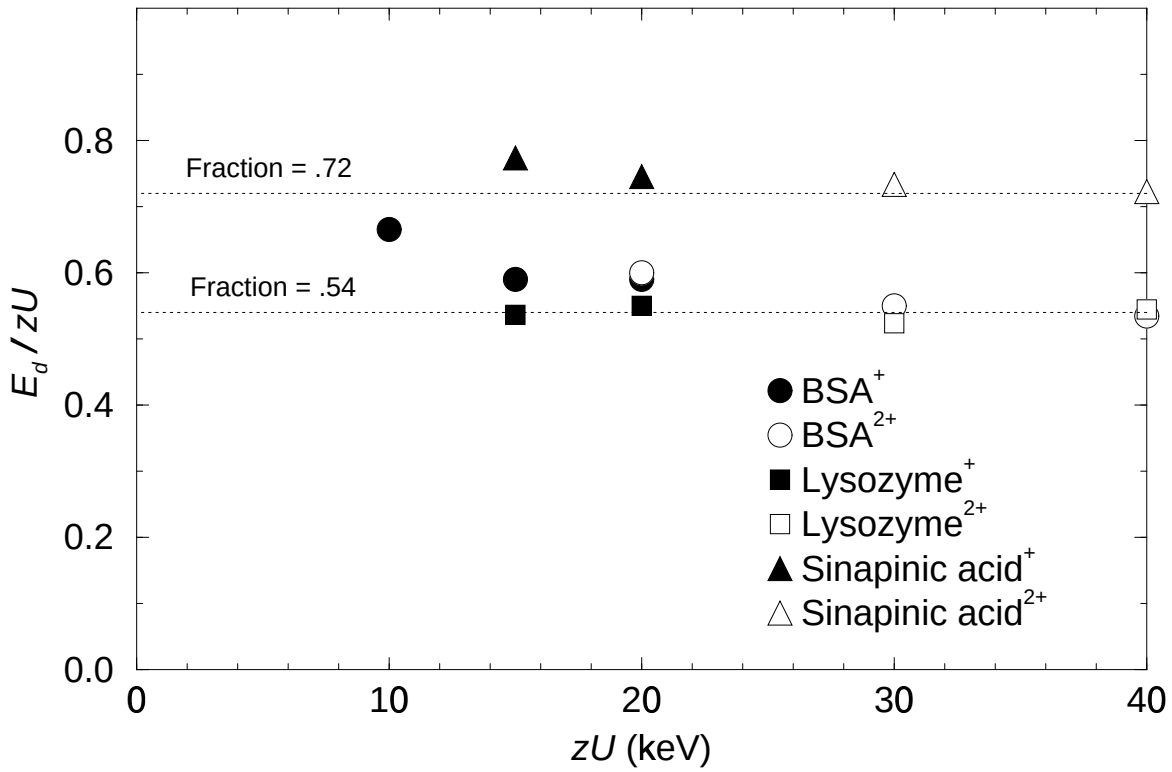
0.8
0.6
0.4
0.2
0.0
0
10
20
30
40
E_d / zU
zU (keV)
Fraction = .72
Fraction = .54
BSA^{+}
BSA^{2+}
Lysozyme^{+}
Lysozyme^{2+}
Sinapinic acid^{+}
Sinapinic acid^{2+}

Figure 3.

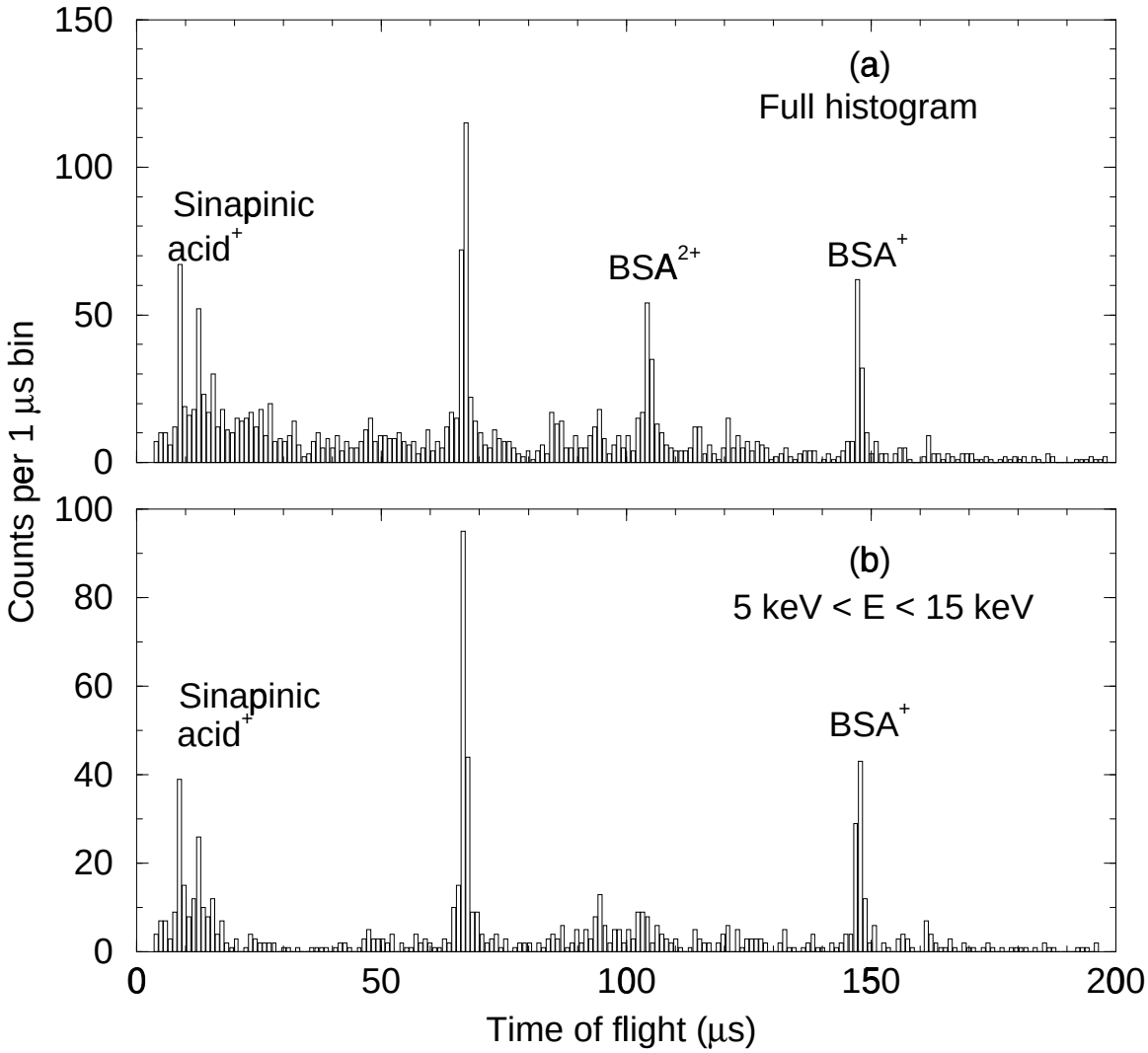
(a)
Full histogram
Sinapinic acid+
BSA2+
BSA+
(b)
5 keV < E < 15 keV
Sinapinic acid+
BSA+
Counts per 1 μs bin
Time of flight (μs)
0
50
100
150
200
0
20
40
60
80
100

Figure 4.

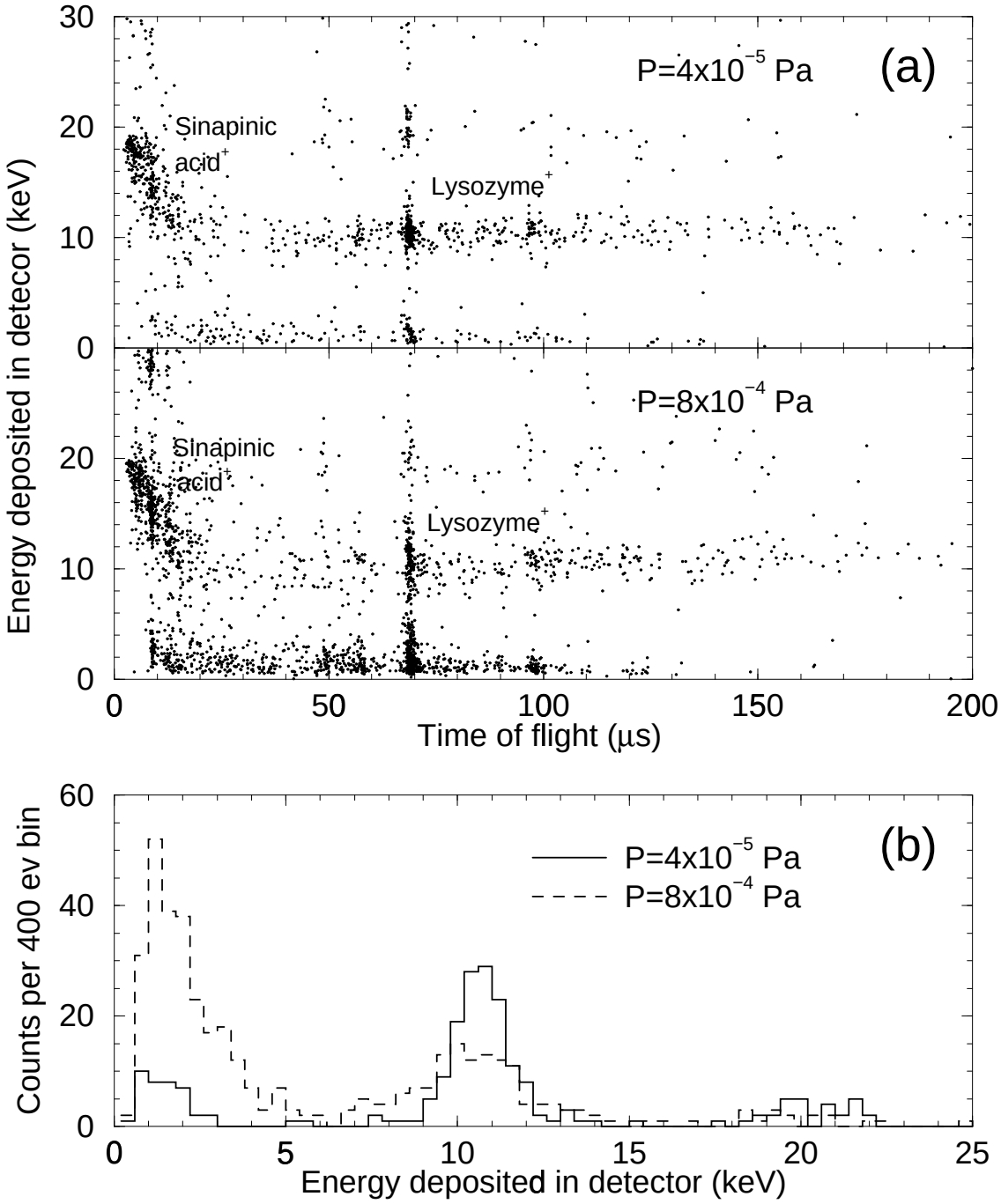
(a)
P=4x10^{-5} Pa
Sinapinic acid$^+$
Lysozyme$^+$
P=8x10^{-4} Pa
Sinapinic acid$^+$
Lysozyme$^+$
Energy deposited in detecor (keV)
Time of flight (μs)
(b)
P=4x10^{-5} Pa
P=8x10^{-4} Pa
Counts per 400 ev bin
Energy deposited in detector (keV)

Figure 5.